



Full-range space-division multiplexing optical coherence tomography angiography

YONGYANG HUANG,¹ JASON JERWICK,^{1,2} GUOYAN LIU,^{1,3} AND CHAO ZHOU^{1,2,4,*} 

¹Department of Electrical and Computer Engineering, Lehigh University, 19 Memorial Drive West, Bethlehem, PA 18015, USA

²Department of Biomedical Engineering, Washington University in St Louis, St Louis, MO 63130, USA

³Department of Dermatology, Affiliated Hospital of Weifang Medical University, Weifang, 261031, China

⁴Department of Bioengineering, Lehigh University, Bethlehem, PA 18015, USA

*chaozhou@wustl.edu

Abstract: In this study, we demonstrated a full-range space-division multiplexing optical coherence tomography (FR-SDM-OCT) system. Utilizing the galvanometer-based phase modulation full-range technique, the total imaging range of FR-SDM-OCT can be extended to >20 mm in tissue, with a digitizer sampling rate of 500 MS/s and a laser sweeping rate of 100 kHz. Complex conjugate terms were suppressed in FR-SDM-OCT images with a measured rejection ratio of up to ~46 dB at ~1.4 mm depth and ~30 dB at ~19.4 mm depth. The feasibility of FR-SDM-OCT was validated by imaging Scotch tapes and human fingernails. Furthermore, we demonstrated the feasibility of FR-SDM-OCT angiography (FR-SDM-OCTA) to perform simultaneous acquisition of human fingernail angiograms from four positions, with a total field-of-view of ~1.7 mm × ~7.5 mm. Employing the full-range technique in SDM-OCT can effectively alleviate hardware requirements to achieve the long depth measurement range, which is required by SDM-OCT to separate multiple images at different sample locations. FR-SDM-OCTA creates new opportunities to apply SDM-OCT to obtain wide-field angiography of *in vivo* tissue samples free of labeling.

© 2020 Optical Society of America under the terms of the [OSA Open Access Publishing Agreement](#)

1. Introduction

The emergence of ultrahigh-speed optical coherence tomography (OCT) [1] with an axial scan (A-scan) rate approaching or exceeding the mega-Hertz (MHz) level has brought in new opportunities for both fundamental biomedical research and clinical applications [2]. Most of these ultrahigh-speed OCT systems have benefited from the rapid development of tunable swept laser sources. However, as the laser sweep rate increases, fewer photons are detected within each sweep, which will ultimately affect the sensitivity of the OCT system [2]. Alternatively, employing parallel-imaging techniques in OCT systems can potentially achieve an equivalent speed improvement. Among parallel-imaging OCT systems, space-division multiplexing OCT (SDM-OCT) [3,4] stands out since it can achieve scalable speed improvement without duplication of the light source, detector, and sample and reference arms. In an SDM-OCT system, a 1xN splitter or multi-layer couplers are used to split the incident beam into multiple beams evenly. Back-scattered interference signals from multiple positions are detected at the same time. An optical delay is introduced between different sampling beams to project OCT signals from different sample locations into different depth ranges. A fiber-based [3] and chip-based [4] SDM-OCT system have been previously demonstrated, with an effective imaging speed of 800,000 axial scans/s (A-scans/s) using eight beam multiplexing. Recently, an ophthalmic SDM-OCT system was successfully demonstrated in a clinical feasibility study [5]. Since multi-channel signals are separated with an optical path length difference (OPD) of a few millimeters between adjacent channels, a long imaging range (>20 mm in tissue) is required for SDM-OCT [4]. To capture OCT images from all channels simultaneously, a wide-bandwidth photodetector, a high-speed

digitizer, and a tunable swept laser with a long coherence length are often used, which increases the system cost and data transfer load for SDM-OCT.

In standard Fourier domain OCT (FD-OCT) systems, interference signals in each A-scan are detected in the form of spectral fringes as a function of wavelength or wavenumber. During post-processing, the sample intensity profiles are reconstructed via inverse Fourier transform (IFT) along the depth direction. Since detected spectral fringes contain real values only, their IFT results are Hermitian [6], which means that they include both sample intensity profiles and their complex conjugates. When sample signals range across the zero delay, they will overlap with their complex conjugates, causing the unwanted blurring of the sample signals. Denoted as complex conjugate ambiguity in literature and commonly found in the FD-OCT system, the issue can be resolved by most full-range techniques in principle. Since these full-range techniques reconstruct the complex representation of spectral fringes, IFT results of the complex spectral fringes will be free of the complex conjugate terms [2]. As a result, the whole imaging range of full-range OCT (FR-OCT) systems can be utilized, which is doubled compared to standard OCT systems. To date, various full-range techniques have been reported to achieve complex signal reconstruction and complex conjugate suppression, including multi-frame acquisition with phase-shifting [7], reference tilting [8], phase modulation with acousto-optic frequency shifter (AOFS) [9] or electro-optic phase modulator (EOM) [10], quadrature detection [11–14], BM-mode scanning [15–17], and galvanometer-based phase modulation [18–21].

In this paper, we incorporated a full-range technique into our SDM-OCT system, denoted as Full-Range SDM-OCT (FR-SDM-OCT). We adopt the galvo-based phase modulation full-range technique [18–20] since no additional hardware is required, yielding a simpler system configuration and easy alignment. Suppression of complex conjugate signals was clearly observed in FR-SDM-OCT, with the complex conjugate suppression ratios measured to be ~46 dB at ~1.4 mm depth and ~30 dB at ~19.4 mm depth using a digitizer sampling rate of 1.0 GS/s and a laser sweeping rate of 100 kHz. Next, we showed that the imaging range of the FR-SDM-OCT system could be extended to >20 mm in tissue when the digitizer was running at 500 MS/s. In the demonstrations of Scotch tapes and human fingernails, sample signals from four positions were fully recovered with an OPD of ~4.5 mm in tissue between adjacent channels. Furthermore, we demonstrated the feasibility of a functional extension of FR-SDM-OCT, FR-SDM-OCT angiography (FR-SDM-OCTA), which can perform simultaneous acquisition of angiograms from four different positions. A stitched FR-SDM-OCT angiogram of the human fingernail was shown in the result, revealing rich details of microvasculature at different depths in both proximal nail fold and nail bed regions. Compared to standard SDM-OCT, FR-SDM-OCT can potentially alleviate the demanding hardware requirements by reducing the digitizer sampling rate, photodetector bandwidth and tunable laser coherence length by half, which may facilitate the wider adoption of SDM-OCT technology.

2. Methods

2.1. Hardware configuration of FR-SDM-OCT

Figure 1(A) shows the schematic diagram of the FR-SDM-OCT system in this study, which is modified from the prototype SDM-OCT system described by Zhou et al. [3]. A vertical-cavity surface-emitting laser (VCSEL, SL1310V1, Thorlabs Inc. USA) was used as the light source, with a spectral range from 1250 nm to 1355 nm and a 3-dB bandwidth of ~80 nm. The laser output power was ~26 mW. A booster optical amplifier (BOA, BOA1130S, Thorlabs) was used after the 97/3 2×2 fiber coupler to amplify the 97% of the laser output from ~24 mW to ~90 mW, with the rest of the power sent to the Mach-Zehnder interferometer (MZI). A 95/5 fiber coupler was used after the BOA to further split the light, with 95% sent to the sample arm and 5% sent to the single-pass reference arm. In the sample arm, a fiber-based SDM component was used to split the incident beam into 4 channels. The actual OPDs between adjacent channels, generated

in the SDM component, were measured to be 6.5 mm, 5.7 mm and 5.8 mm in air, respectively. The four output beams are first converted to collimated beams with an infinity-corrected objective (M Plan Apo, 20 \times , Mitutoyo). Two relay lenses (AC508-100-C, $f = 100$ mm, Thorlabs) were used to converge the four collimated beams at the first mirror of the galvanometer (Galvo). The diameter of each collimated beam was ~ 2 mm. An achromatic doublet (AC-254-040-C, $f = 40$ mm, Thorlabs) was used as the objective lens, yielding the final spacing between adjacent channels to be ~ 1.8 mm. The sample power of each beam was measured to be ~ 8 mW. The single-pass reference arm was built with two collimators, with one collimator fixed, and the other collimator mounted on a 1D translational stage to adjust the relative optical delays between the sample and reference arms. The free-space optical path of the reference arm was matched to twice the optical path of the sample arm. The reference arm power was controlled at >700 μ W to achieve shot-noise-limit detection. The sample and reference signals interfered at the 50/50 fiber coupler before they were detected by a dual balanced detector (DBD, PDB480C-AC, Thorlabs). Back-coupling power at one port of the 50/50 fiber coupler was measured to be ~ 300 μ W. Interference signals from the detector were digitized by a high-speed digitizer (ATS9373, Alazar Technologies Inc.). Axial and lateral resolutions were measured to be ~ 12 μ m and ~ 14 μ m in air, respectively.

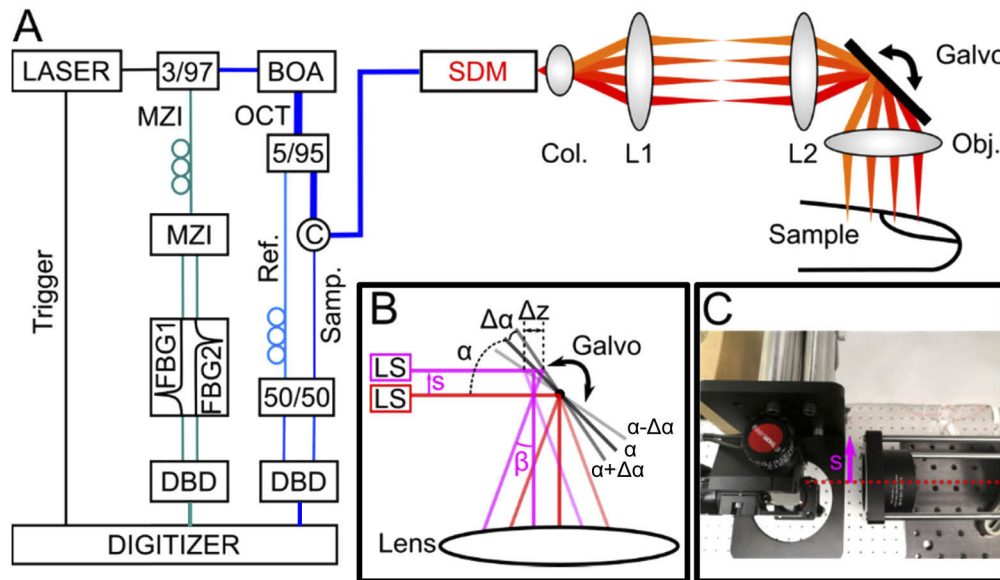


Fig. 1. (A) Schematics of Full-range Space-division Multiplexing OCT (FR-SDM-OCT). (B) Schematic illustration of galvo-based full-range technique. Only one incident beam is shown. Red: original path. Magenta: Offset path. (C) Realization of beam offsetting (s) in FR-SDM-OCT system. BOA: Booster optical amplifier; C: Collimator; DBD: Dual balanced detector; FBG: Fiber Bragg grating; Galvo: Galvanometer; L1, L2: Lens; LS: light source; MZI: Mach-Zehnder interferometer; Obj.: Objective; Ref.: Reference arm; Samp.: Sample arm; SDM: Space-division multiplexing component.

2.2. Galvo-based phase modulation full-range technique

Figure 1(B) shows the schematic illustration of the galvo-based full-range technique, which was first introduced and well summarized by Baumann et al., Leitgeb et al., and An et al. [18–20]. By shifting the incident beam of the pivot axis of the fast mirror of the galvanometer, changes of the optical path length (Δz) were created during lateral scanning, yielding constant phase

modulation between neighboring axial scans. In the post-processing steps, a Hilbert transform was applied to digitally reconstruct the analytic complex representation of spectral fringes. In this work, we are adapting the galvo-based full-range technique demonstrated in [18] and others in our SDM-OCT system to address the challenges related to high data throughput. Figure 1(C) shows the realization of beam offsetting in the FR-SDM-OCT system.

In Fig. 1(B), three mirror positions are presented with different transparency levels, with mirror rotation angles of α (dark), $\alpha + \Delta\alpha$ (normal) and $\alpha - \Delta\alpha$ (light). Red lines show the original light path with the beam incident on the pivoting axis. The three reflected beams indicate the reflection directions corresponding to different mirror positions, with a scanning angle at β , 0, and $-\beta$. From the law of reflection, we can get:

$$\beta = 2\Delta\alpha \quad (1)$$

The unmodulated OCT interference signals (spectral fringes) are expressed as:

$$I(k, x) \sim S(k, x) \sum_n (\sqrt{\alpha_r \alpha_n} \cos(2z_n \cdot k)) \quad (2)$$

where fringe signals $I(k, x)$, source spectra $S(k, x)$ and phase term $\cos(2z_n \cdot k)$ are functions of wavenumber k and transverse scanning parameter x .

When the galvo-based full-range technique is employed, the incident beam is offset from the pivoting axis. In Fig. 1(B), magenta lines indicated the offset light path, of which the incident beam is shifted by s (distance). When the galvo-mirror scans from one side to the other, the change of the sample arm optical path length (OPL, Δz) can be approximated as:

$$\Delta z \approx 2 \frac{s}{\sin\alpha} \cdot \Delta\alpha \cdot \frac{1}{\sin\alpha} = \frac{s \cdot \beta}{\sin^2\alpha} \quad (3)$$

In a general setting of the galvanometer, $\alpha = 45^\circ$. $\sin^2\alpha = 1/2$. Thus

$$\Delta z \approx 2\beta s \quad (4)$$

Offsetting the incident light on the galvo mirror will introduce a phase modulation term $\phi(x)$, which is related to the transverse scanning parameter x :

$$I(k, x) \sim S(k, x) \sum_n (\sqrt{\alpha_r \alpha_n} \cos(2z_n \cdot k + \phi(x))) \quad (5)$$

Note that we can use the index of the A-scan in the B-scan to represent the transverse scanning parameter, which is denoted as m . Thus, $\phi(x)$ can be expressed as $\phi(m)$. The total number of A-scans in a B-scan is denoted as M . The total phase change in a B-scan could be derived as:

$$\phi(M) = 2k\Delta z = \frac{4\pi \cdot s \cdot 2\beta}{\lambda} \sim \frac{4\pi \cdot s \cdot x_M}{\lambda \cdot F} \quad (6)$$

Where x_M represents the transverse (lateral) scan range, and F is the focal length of the objective lens.

The modulation frequency u for the galvo-based phase modulation can be defined as the phase change between neighboring axial scans [20]. Since:

$$\phi(M) = u \cdot M \quad (7)$$

We can get:

$$u = \frac{\phi(M)}{M} \sim \frac{4\pi \cdot s \cdot x_M}{\lambda \cdot F \cdot M} \quad (8)$$

Therefore, the modulation frequency u is proportional to beam offset s and transverse scan range x_M (which is determined by the input voltage to the galvo mirror), and inversely proportional

to the number of axial scans (M) in one B-scan. With a properly value set of s , x_M and M , the amount of the phase modulation can be controlled to optimize the complex conjugate suppression [18,20].

2.3. Post-processing procedures for FR-SDM-OCT and FR-SDM-OCTA

2.3.1. Post-processing procedures for standard SDM-OCT

Figure 2(A)–2(D) illustrates flow charts of the post-processing procedures for both standard and full-range SDM-OCT systems. Figure 2(A) shows the post-processing procedure for standard SDM-OCT systems, which is similar to the procedure described in Huang et al. [4]. The following steps are included: Residual DC removal, zero-padding, data resampling, dispersion compensation, application of Gaussian window, and the final inverse FFT along the axial direction.

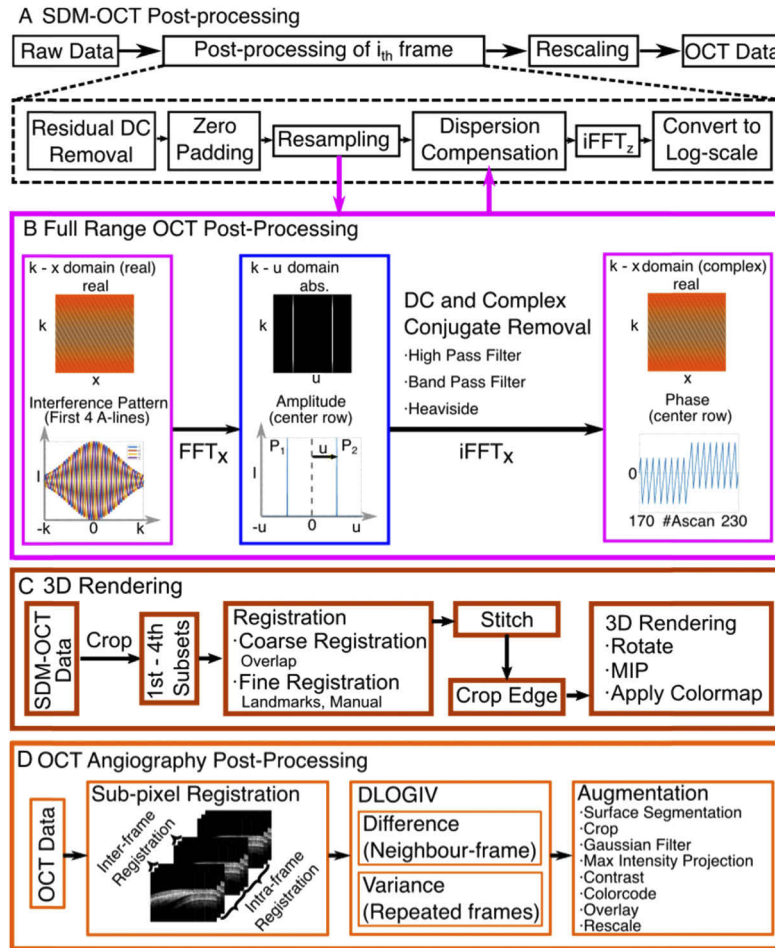


Fig. 2. Flow chart of the post-processing procedures for standard SDM-OCT (A), additional step for full-range SDM-OCT (B), 3D rendering (C), and OCT angiography (D).

2.3.2. Digital reconstruction of the complex OCT interference signals

For the digital reconstruction of complex interference signals for FR-SDM-OCT, additional post-processing steps are performed right after the linear data resampling step of the standard SDM-OCT procedures, which are also well described in previous studies [18–20]. These steps

are shown in the magenta rectangular box in Fig. 2(B). In the first step, a 1D fast Fourier transform (FFT) is performed on a linear sampled 2D OCT data (B-scans), along the fast-axis scanning direction (X direction), for each wavenumber k . When the full-range imaging is applied, the image peak (P2) and its complex conjugate peak (P1) are separated by twice of the modulation frequency (u) due to galvo-based phase modulation. Next, a filter is applied on each row to filter out at least half of the spectrum to remove the complex conjugate peaks (P1). The filter could be a high-pass filter, band-pass filter, or a Heaviside function. In this study, a band-pass filter is used. After this step, an inverse FFT is performed along the transverse direction to convert the 2D OCT data from $k - u$ domain back to $k - x$ domain to reconstruct the analytic complex representation of the OCT interference signals. Afterward, the rest of the standard SDM-OCT post-processing procedures can be applied.

We should point out that SDM-OCT λ - k conversion (data resampling) and the galvo-based full-range demodulation analysis (digital reconstruction) can be treated as two independent steps. The multi-channel SDM-OCT signals are encoded along the z direction and analyzed altogether. It won't be affected when performing Fourier transforms from x domain to u domain, or from u domain back to x domain, which is the key of the galvo-based full-range OCT scheme. During these transforms along the horizontal (x) direction, the $k \cdot z$ term of the phase in Eq. (5):

$$\cos(2z_n \cdot k + \phi(x)) = \frac{1}{2} [\exp(i \cdot 2z_n \cdot k) \exp(i\phi(x)) + \exp(-i \cdot 2z_n \cdot k) \exp(-i\phi(x))] \quad (9)$$

is treated as a constant.

2.3.3. 3D rendering procedures

Figure 2(C) describes the post-processing procedures to generate the 3D rendered images from the reconstructed SDM-OCT data. First, the reconstructed 3D SDM-OCT data are cropped into four subsets containing images from each individual channel, based on the depth ranges. Second, two-step rigid registrations are performed to align these four subsets. A coarse registration is performed along the slow-axis direction between subsets from adjacent beams, based on the known percentage of overlaps between them. The overlap percentage is equal to $(1 - 1.8 \text{ mm} / \text{slow-axis scan range in mm}) \times 100\%$. Then, a fine registration is performed between these two subsets along all three directions, based on the structural landmarks in the overlap region, e.g. surface contour. Note that no rotation is involved in the two-step registrations. Once all four subsets are well-registered, they are stitched together to form a single 3D data. The blank regions close to the edge of the stitched 3D data are cropped. From the stitched 3D data, we can generate the 3D rendered image of the sample by rotating the data, performing maximum intensity projection (MIP), and applying the color map. In our study, the 3D rendered image (Fig. 7(F)) is generated by Amira (FEI, now part of ThermoFisher).

2.3.4. Post-processing procedures for FR-SDM-OCTA

The flow chart of post-processing procedures for FR-SDM-OCTA is illustrated in Fig. 2(D), following an improved speckle variance OCT method, named differential logarithmic intensity variance (DLOGIV), which was demonstrated by Motaghianezam et al. [22]. After OCT data are generated following standard or full-range SDM-OCT post-processing procedures, a two-step subpixel registration [23], involving an inter-frame registration on repeated frames and an intra-frame registration on frames from different slow-axis locations, is performed to align all the B-scans. This step facilitates the suppression of dynamic signals from the micron-scale translational sample motion, yielding a better contrast of flow signals. Next, DLOGIV is employed from each stack of repeated frames to extract the flow information at each slow-axis location. After all the frames were processed, *en face* OCT angiograms are generated and optimized with additional augmentation steps listed in Fig. 2(D).

To generate an overlaid angiogram on top of the corresponding gray-scale B-scan image, the following procedures are performed. First, the B-scan angiogram is generated, normalized by dividing by the max intensity of the B-scan angiogram and multiplying by 255. Second, an intensity threshold is applied to the angiogram to remove some background signals. Then, the overlaid image is generated by merging RGB channels, using the thresholded angiogram image as the red channel and B-scan image as the green and blue channels.

2.3.5. Data resampling and phase stabilization

For SS-OCT, detected spectral fringes may not be linearly sampled as a function of wavenumber, since tunable swept lasers may not be linearly swept across the whole wavenumber (wavelength) range. In our work, simultaneous acquisitions of both OCT and MZI spectral fringes are employed. Especially, since the MZI provides consistent, periodic sinusoidal spectra, each MZI signal is used to construct a phase curve to perform linear resampling for the corresponding OCT fringe [3,24].

The phase stability of the SDM-OCT system is critical for the galvo-based full-range demodulation analysis. Thus, the phase calibration and data resampling steps should be performed prior to the digital reconstruction step to ensure a successful reconstruction of analytic complex OCT interference signals. One common issue for SS-OCT is trigger jitter, in which data acquisitions of OCT/MZI spectral fringes exhibits sweep to sweep variations, i.e. starting from different wavelengths, yielding the irregular movements of spectral ranges for different OCT/MZI fringes and corrupted phase relationships between adjacent sweeps or A-scans [25,26]. Illustrations of the trigger jitter phenomenon for SDM-OCT are shown in Fig. 3(A)–3(B). A fiber Bragg grating (FBG) was inserted in the MZI channel to filter out a narrow band and generate a sharp FBG peak in each MZI fringe. Figure 3(A) shows multiple MZI fringes. In the zoomed MZI fringes within the red rectangle regions from Fig. 3(A), trigger jitter was easily identified as the spectral range of the FBG peaks were moving irregularly for different laser sweeps (Fig. 3(B)). In previous studies, the trigger jitter can be resolved by using the split, FBG-filtered source signals as the acquisition trigger (λ - trigger) [26,27], using an FBG to generate a sharp peak in each OCT fringe as a timing reference [25] and a fixed range of accumulated MZI phase to crop each pair of OCT and MZI spectra and perform data resampling [24]. The data resampling technique employed in this study is adapted from previous work [24,25]. First, two FBGs are added to the MZI, one for each output port of the MZI (Fig. 1(A)). A representative screenshot of both OCT (pink) and MZI (green) fringes is shown in Fig. 3(C), with two FBG peaks in opposite directions labeled in the MZI channel. The first FBG is centered at ~ 1350 nm, and the second FBG is centered at ~ 1253 nm, which are close to the beginning and the end of the swept wavelength range of the VCSEL. Both FBGs have a narrow filter bandwidth (< 1 nm). Next, we use the accumulated MZI phase range between these two FBG peaks to crop each pair of OCT/MZI fringes and to

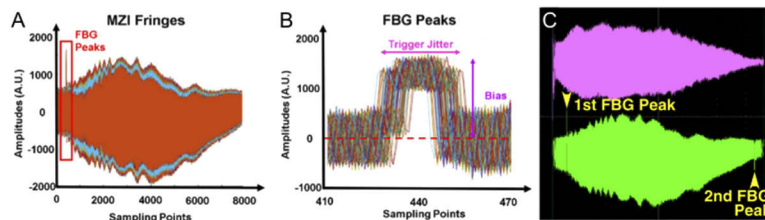


Fig. 3. (A-B) Illustration of trigger jitter in MZI signals from different laser sweeps (A-scans). (B) is the zoomed view of the red rectangle region in (A). (C) A screenshot of representative OCT (pink) and MZI (green) fringes, using two FBG peaks in the MZI channel for a correct phase calibration.

generate the correct phase calibration curve for the OCT fringe to perform λ - k conversion (data resampling). Since the wavelength (wavenumber) range between these two FBG peaks is known and fixed, we can guarantee that all sweeps are well aligned, resolving trigger jitter issue. Since the accumulated MZI phase ranges determined by this technique are quite consistent among all sweeps, signal frequencies in k domain after interpolation remains consistent for all sweeps, ensuring consistent measured sample positions (especially in deeper depth ranges) during Fourier transforms along the z direction and consistent phase changes between adjacent A-scans.

3. Results

3.1. Characterization of full-range imaging in SDM-OCT

To show the feasibility of full-range detection, we first utilized FR-SDM-OCT to image a mirror, with a neutral density filter ($OD = 2.0$) added in the sample arm. In this demonstration, the digitizer sampling rate was set to 1.0 GS/s, which ensured that images from four channels were all included and sufficiently separated within a total imaging range of >20 mm in air. To enable full-range detection, the beam offset s was ~ 3 mm, the scan range x_M was ~ 1.5 mm and the number of effective A-scans M was 750. After mirror images were acquired, fringe signals were processed by both standard and full-range SDM-OCT post-processing procedures (Section 2.3), respectively. Figure 4(A) shows the standard 1×4 SDM-OCT mirror image. Mirror images from 4 different channels (labeled in Fig. 4(A)) were observed separated in positive depth ranges, while their corresponding complex conjugates were shown in the negative depth ranges. Figure 4(B) shows the intensity profile across the central row of Fig. 4(A). Due to the dispersion compensation used in both standard and full-range SDM-OCT post-processing procedures [28], mirror images in the positive depth ranges maintained their sharp peaks while the corresponding complex conjugate peaks were broadened with lower peak intensity. This results in a misleading visualization where the complex-conjugate peaks appear brighter in Fig. 4(A). Acquired at the same mirror positions, Fig. 4(C) shows a full-range 1×4 SDM-OCT mirror image, with the corresponding central-row intensity profile shown in Fig. 4(D). Compared to Fig. 4(A) and 4(B), complex conjugate peaks in the negative depth ranges were significantly suppressed. Especially, at -1.4 mm depth, the 1st complex conjugate peak was almost fully suppressed compared to the first peak in the positive depth range. Although not fully suppressed, the 2nd, 3rd, and 4th complex conjugate peaks in Fig. 4(D) were significantly lower than the corresponding mirror peaks.

To quantify the suppression of complex conjugate peaks, complex conjugate rejection ratios (CCRRs) were measured for each pair of mirror images and their complex conjugates in Fig. 4(B) and 4(D), which were the peak difference between the two in the log-scale intensity profile. In Fig. 4(B), CCRR of the 1st mirror peak was measured to be 11.1 dB, and CCRR of 4th mirror peak was 9.0 dB. These CCRRs observed in standard SDM-OCT were attributed to dispersion compensation [28]. In Fig. 4(D), CCRRs of >46.1 dB, and ~ 30.0 dB were measured for the 1st and 4th mirror peaks, respectively. Excluding the dispersion compensation effect by taking the difference of CCRR values in Fig. 4(B) and 4(D), CCRRs due to galvo-based full-range technique were 35.0 dB and 21.0 dB for the 1st and 4th mirror peaks, respectively. As the OPD increased from 0 to ~ 20 mm, complex conjugate suppression due to galvo-based full-range technique became less effective.

3.2. Characterization of phase modulation with various parameters for FR-SDM-OCT

In Section 2.2, we show that three parameters, including beam offset s , transverse scan range x_M and the number of A-scans per B-scan M , can be altered to control phase modulation. To characterize the phase modulation experimentally with FR-SDM-OCT, we measured the modulation frequencies u in the FFT_x spectra, which were generated from acquired FR-SDM-OCT images of a Scotch tape. Specifically, we examined the relationships between u and these

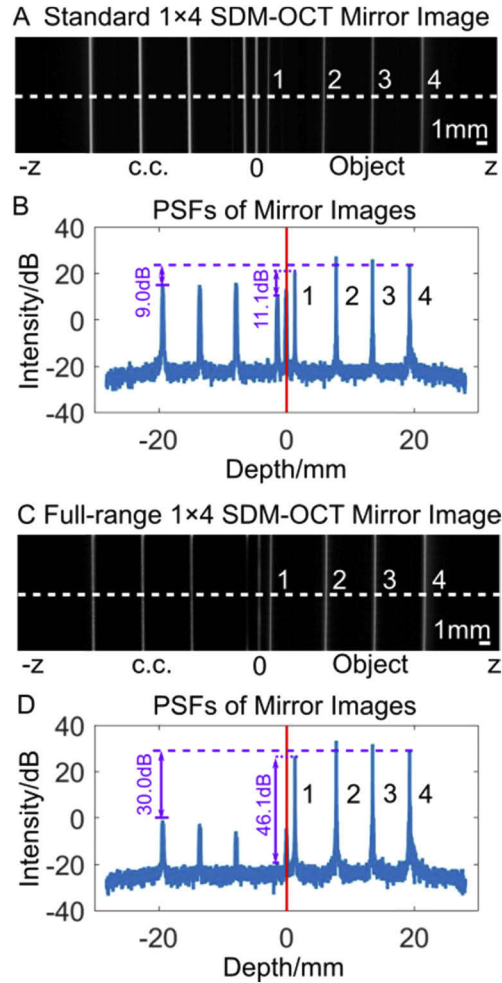


Fig. 4. Mirror images from standard and full-range SDM-OCT. Sampling rate was 1.0 GS/s. (A) and (C) were four-channel mirror images taken from a standard or a full-range SDM-OCT system. (B) and (D) were intensity profiles across the center rows of (A) and (C). Complex conjugate rejection ratio (CCRR, in dB) of the 1st and the 4th peaks were shown in (B) and (D). Scale bar: 1 mm.

parameters by changing one parameter at a time. These results are summarized in Fig. 5. Figure 5(A)–5(B) show the experimental results of u as a function of beam offset s . In Fig. 5(A), center rows of 2D FFT_x spectra (in $k - u$ domain) at various s all show the separation of images and their complex conjugate peaks, indicating the effects of phase modulation. As s was tuned from ~1 mm to ~5 mm, the phase modulation increased, indicated by the increased separation of signal and complex conjugate peaks. Figure 5(B) shows a linear fitting result of u as a function of s . In this sub-figure, modulation frequencies u were first calculated as half of the absolute peak distance between the image and complex conjugate peaks. Then, they were normalized to the maximum spatial frequencies so that they were in the range of (0, 1). A high linear correlation ($R^2 = 0.9879$) was found between u and s for all the five beam offsets, showing the agreement with Eq. (8) in Section 2.2. Figure 5(C)–5(D) show the relationship between the modulation frequency u and transverse scan range x_M . In Fig. 5(C), an increasing separation between images and complex conjugate peaks were observed in center rows of FFT_x spectra as

x_M increased from ~ 0.5 mm to ~ 2.5 mm. Similarly, the linear fitting result (Fig. 5(D)) shows a high linear correlation ($R^2 = 0.9999$) between these two parameters. Characterization results of the relationship between modulation frequency u and the number of A-scans per B-scan M are shown in Fig. 5(E)–5(F). As opposed from the cases of various s and x_M , the separation of image and complex conjugate peaks decreases in the center rows of 2D FFT_x spectra as M was increased from 450 to 850 A-scans (Fig. 5(E)). Based on Eq. (8), a linear fitting was performed between u and the reciprocal of M ($1/M$). In the fitting result (Fig. 5(F)), a high correlation ($R^2 = 0.9999$) between u and $1/M$ was confirmed. Figure 5 demonstrated that the beam offset s , the transverse scan range x_M and the number of A-scans per B-scan M can be changed to change the phase modulation in order to optimize the performance of FR-SDM-OCT.

3.3. Full-range SDM-OCT Applications with Half Sampling Rate

To demonstrate the feasibility of the full-range technique in SDM-OCT, we employed FR-SDM-OCT to image a Scotch tape and a human fingernail, using a sampling rate that is half of the required sampling rate for standard SDM-OCT. Figure 6 shows the results of FR-SDM-OCT imaging of Scotch tape with a digitizer sampling rate of 0.5 GS/s. In the standard 1×4 SDM-OCT image (Fig. 6(A)), Scotch tape images from 1st to 4th channels (red labels) overlapped with their complex conjugates. In the $3 \times$ zoomed image from the red rectangular region of Fig. 6(A) (Fig. 6(C)), the mirrored complex conjugate image from the 2nd channel was clearly visible and partially overlapped with the tape image from the 3rd channel, resulting in a blurry overlapping region and unresolvable layered tape structure. In comparison, in the full-range image layered tape structures were clearly distinguishable for all four channels (Fig. 6(B)). The $3 \times$ zoomed view of the yellow rectangular region from Fig. 6(B) clearly shows that the complex conjugate image from the 2nd channel was fully suppressed (Fig. 6(D)). We should note that, due to strong surface scattering of the tape, some residual signals from the 1st, 3rd, and 4th complex conjugate images remained visible in Fig. 6(B) (White arrows), although they had been suppressed by >30 dB.

In Fig. 7, *in vivo* FR-SDM-OCT images of a human fingernail are shown, which were obtained with the same digitizer sampling rate of 0.5 GS/s. In Fig. 7(A), images of the fingernail from four channels were rendered in separated depth ranges. The total imaging range enabled by the full-range technique was measured to be ~ 21 mm in tissue, assuming a refractive index of 1.33. Figure 7(B)–7(E) show the $2 \times$ zoomed views of the fingernail from the 1st to 4th beams, respectively. Since the alignment of four incident beams was in parallel to the boundary of the nail junction (NJ), the nail junction structure was visible in all these zoomed images. In the proximal nail fold (PNF), the dermal/epidermal junction (DEJ) was clearly visible. In Fig. 7(C) and 7(D), the cuticle that extruding out from the epidermis of the proximal nail fold was shown. A clear separation of the nail plate (NP) and nail bed (NB) was observed, indicated by the high-scattering interface between these two regions. Following procedures in Section 2.3.3, a 3D rendered fingernail was reconstructed, which was shown in Fig. 7(F). In all these zoomed images, most of the complex conjugate signals were suppressed effectively by the full-range technique, although some residue signals from the high-scattering skin surface remained (yellow arrow). Additional artifacts were observed, indicated by orange arrows on top of the 1st beam image in Fig. 7(A), and Fig. 7(B). They were identified as aliased high-frequency back-scattered signals from the 4th beam, caused by a combination effect of multi-scattering of the thick fingernail, non-linear data sampling, and a large optical delay of 4th beam image relative to the zero-delay position (indicated with a red 0 in Fig. 7(A)).

3.4. Full-range SDM-OCT angiography (FR-SDM-OCTA)

Here, we demonstrate the feasibility of FR-SDM-OCT angiography (FR-SDM-OCTA). Figure 8 shows representative results of angiograms of a human fingernail with the FR-SDM-OCT. During the acquisition, 600 axial scans were captured in each frame, yielding a frame rate of ~ 140 Hz

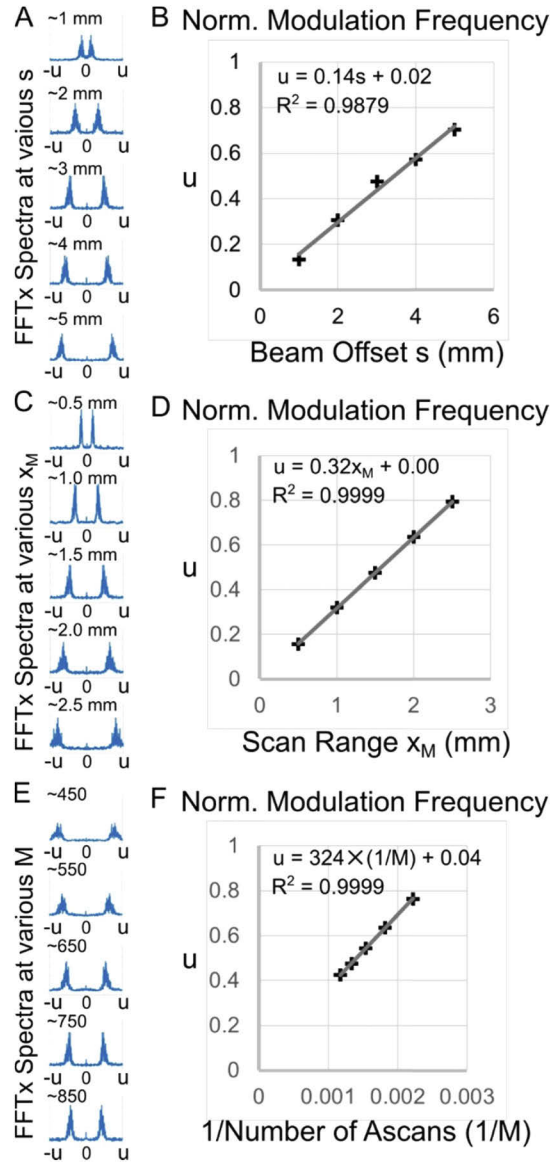


Fig. 5. Experimental observation of phase modulation as function of various parameters, including beam offsets (s), transverse scan range x_M and number of effective A-scans M . (A - B) Phase modulation at various s . $x_M \sim 1.5$ mm. $M = 750$. (A) Center rows of FFT_x spectra at various s . (B) Linear fitting between normalized modulation frequency u and s . (C - D) Phase modulation at various x_M . $s \sim 3$ mm. $M = 750$. (C) Center rows of FFT_x spectra at various x_M . (D) Linear fitting between u and x_M . (E - F) Phase modulation at various M . $s \sim 3$ mm. $x_M \sim 1.5$ mm. (E) Center rows of FFT_x spectra as a function of M . (F) Linear fitting between u and $1/M$.

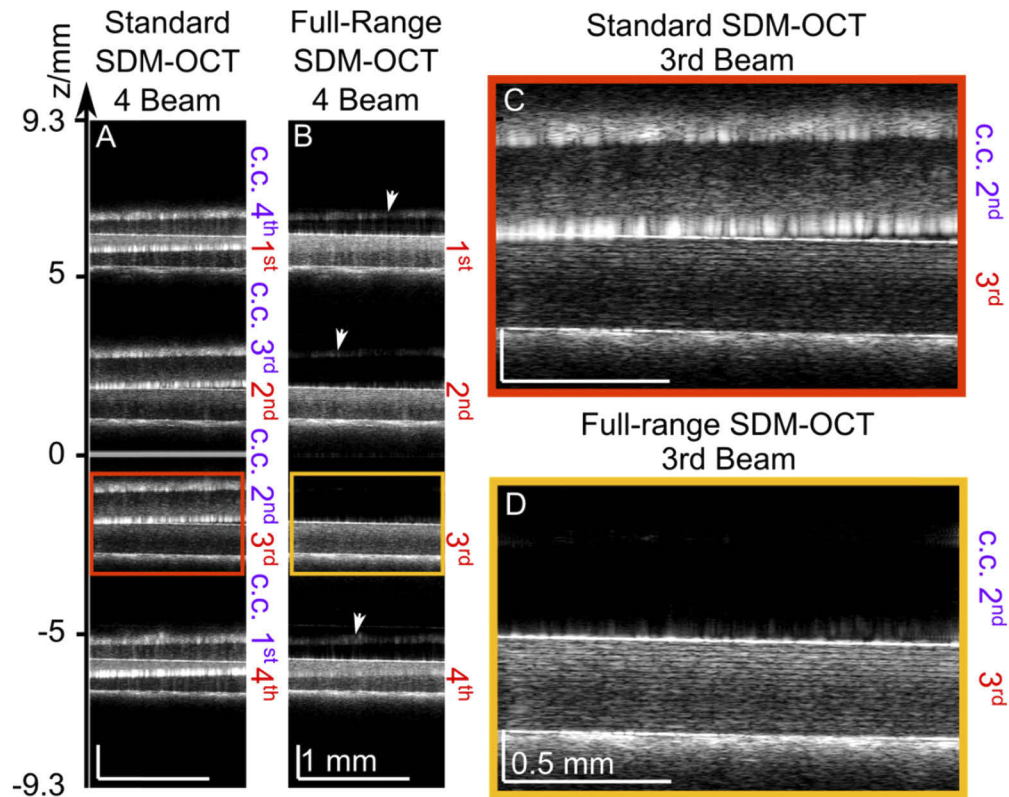


Fig. 6. A comparison between standard and full-range SDM-OCT images of a Scotch tape. Sampling rate was 0.5 GS/s (half sampling rate). (A) 1×4 standard SDM-OCT image, showing overlapping of sample and complex-conjugated images. (B) 1×4 FR-SDM-OCT image, showing clear tape structure with significant suppression of complex conjugate images. (C, D) 3× zoomed views of tape images from the 3rd beam in (A) and (B). Red and magenta labels on the right side of each sub-figure indicated the channels of the sample images and their complex conjugates. White arrows: residual complex conjugate signals. Scale bar: 1 mm for (A - B) and 0.5 mm for (C, D).

with an 85% duty cycle for each frame. In the slow axis, each volume consisted of 300 frames, and eight repeated frames were acquired at each Y location. Using four-channel multiplexing, the equivalent total number of A-scans was 5.76 million ($600 \times 300 \times 8 \text{ repeats} \times 4 \text{ channels}$). The total imaging time was ~ 17 s. The final scan area of the fingernail was $\sim 1.7 \times \sim 7.5 \text{ mm}^2$, after manual stitching and edge cropping. In order to achieve full-range detection, the beam offset was set to be ~ 2 mm. Figure 8(A) shows a photograph of the volunteer's index finger and orientation of four beams on the fingernail. Figure 8(B) shows the stitched cross-sectional FR-SDM-OCT image of the fingernail, showing the structure of the nail junction similar to the observations in Fig. 7. The corresponding angiogram was highlighted in the red channel and overlaid on top of the structural image, following the procedures described in Section 2.3.4. Large vessels were observed in the dermal region of the proximal nail fold and the nail bed region. Figure 8(C) is the stitched FR-SDM-OCT angiogram of the nail junction, which is generated by surface flattening, coloring-coding the angiogram by imaging depth from the skin surface and performing maximum intensity projection. The complexity of the microvascular network in both proximal nail fold and nail bed regions can be appreciated. Although 8 repeated frames were utilized to generate a B-frame angiogram and subpixel registration was performed to correct motion artifacts,

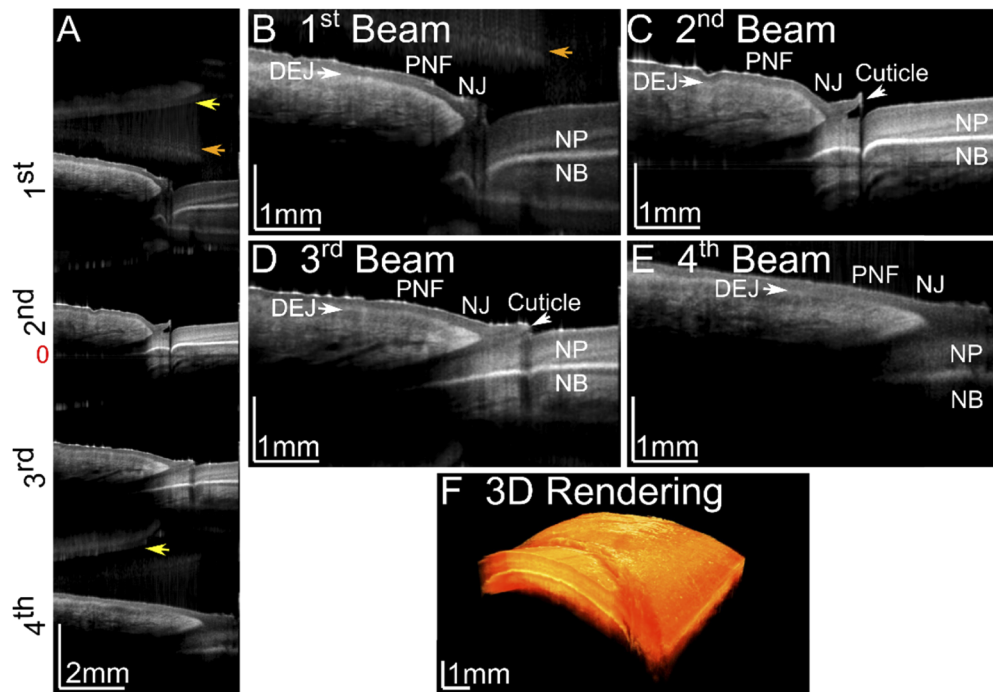


Fig. 7. FR-SDM-OCT images of the human fingernail *in vivo*. Sampling rate was 0.5 GS/s. The full FR-SDM-OCT image were shown in (A). Four fingernail images were displayed separately in a total depth range of ~21 mm. (B -E) 2× zoomed images of each beam from (A). Proximal nail fold (PNF), nail junction (NJ), dermal/epidermal junction (DEJ), cuticle, separation of nail plate (NP) and nail bed (NB) were clearly visible. Yellow and orange arrows in (A) and (B): artifacts. (F) 3D rendering of scanned region of the fingernail. 0 in red: Zero delay. Scale bar: 2 mm for (A) and 1 mm for (B-E).

these steps might not be sufficient to completely remove the motion artifacts, resulting in some transverse stripes shown in Fig. 8(C). Figure 8(D)–8(H) show FR-SDM-OCT angiograms from five layers located at different depth ranges, which were labeled in each sub-figure. Small vessels were observed between 200 - 1000 μm below the surface of the proximal nail fold and between 600 - 1200 μm below the nail surface. Below these regions, the vessels could not be distinguished from the noise floor. We should note that a disrupt cutoff of the microvascular network at the edge of the cuticle region was detected in Fig. 8(F). The cutoff was due to surface discontinuity between cuticle and nail bed regions during the surface flattening procedure, which resulted in a disconnected microvascular network. Figure 8(I)–8(M) summarize representative features of microvascular layers in different skin layers observed by FR-SDM-OCTA, which are extracted from Fig. 8(D)–8(H). Figure 8(I) shows the papillary layer (PL) of microvasculature, which can be observed near the DEJ between ~200 - 600 μm below the surface of the PNF. At the distal end of the PNF, capillaries appeared to be near-parallel, elongated lines, oriented perpendicular to the border of the nail junction in the MIP OCT angiogram (also see Fig. 8(D)). These features in PL were also well examined by Sangiorgi et al. [29] under scanning electron microscopy (SEM) and Baran et al. [30] under the OCT. Due to the limited lateral resolution, the elongated capillary loops appeared as a line in Fig. 8(H). Below PL, the sub-papillary layer (SPL) was observed in the OCT angiograms (Fig. 8(J)), with a clear feature of a meshed network structure filled with medium-size vessels. Underneath, a large vessel originating from a deeper layer and its distal branches were connected to the SPL (Fig. 8(G) and 8(H)), which was a representative

feature of the reticular layer (RL, Fig. 8 K). In the nail bed, the pseudo-papillary layer (PPL), the uppermost microvascular layer close to the nail junction, is shown in Fig. 8 K, which is similar to the papillary layer of PNF. However, orientations of these parallel capillaries were along the major axis of the nail instead of perpendicular to the border of the nail junction (See Fig. 8(C)). In the literature, these capillaries are originated from the nail root and connected to the nail bed [29]. Under PPL, SPL was also found in the nail bed (Fig. 8(L)). Bifurcation and cross-links of medium-size micro-vascular vessels were clearly observed in this layer.

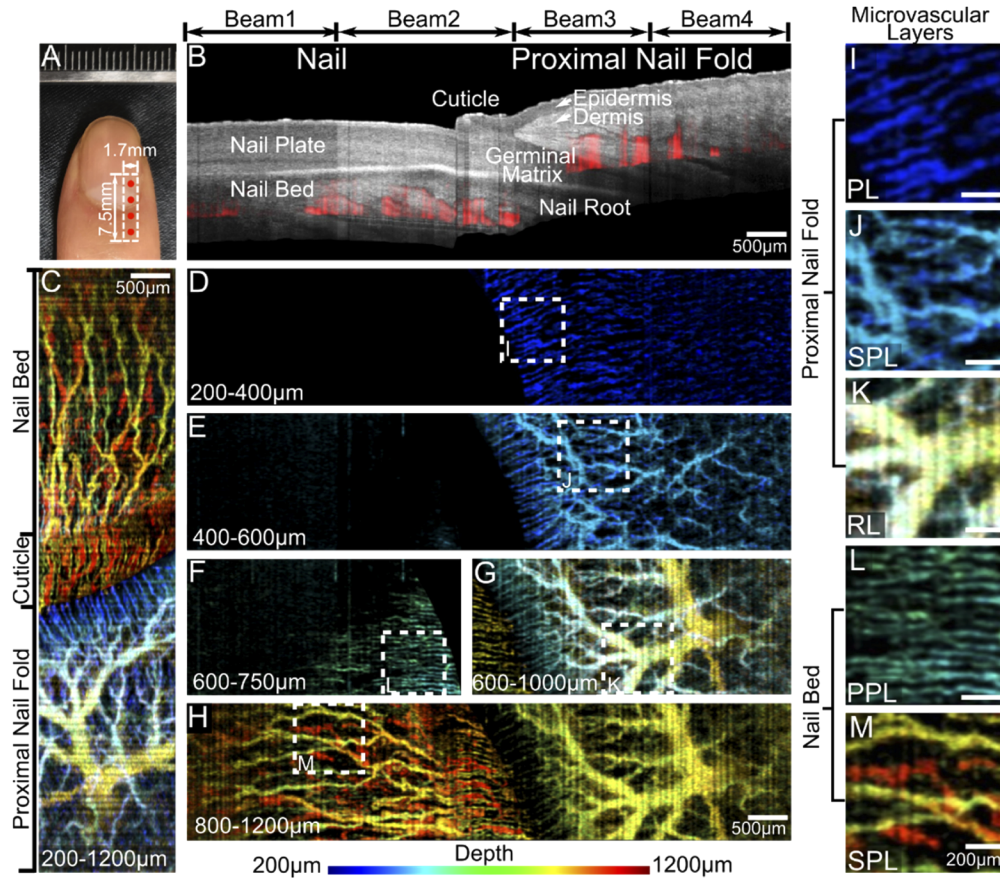


Fig. 8. FR-SDM-OCT angiograms of the human fingernail junction. (A) A photograph of volunteer's index finger. Four parallel channels were shown in the white rectangular box, covering a scan area of $\sim 1.7 \text{ mm} \times \sim 7.5 \text{ mm}$. (B) Stitched, cross-sectional FR-SDM-OCT image of the fingernail junction, with the corresponding angiogram overlaid on top of the structural image in the red channel. (C) Depth-encoded FR-SDM-OCT angiograms of the fingernail, merged from a depth range of 200-1200 μm below the surface. (D-H) Five representative FR-SDM-OCT angiograms showing the microvascular networks at different layers. (I-M) Zoomed microvascular layers in the proximal nail fold and nail bed. PL: papillary layer; SPL: sub-papillary layer; RL: reticular layer; PPL: pseudo-papillary layer. Scale bars: (B - H) 500 μm ; (I - M) 200 μm

4. Discussions

Full-range techniques have been applied in SD-OCT systems to resolve the complex conjugate ambiguity and to expand total depth ranges [18,19]. For SS-OCT system, full-range techniques

are less appreciated since the total imaging range of most swept-source OCT systems is more than enough to cover the sample image with a light penetration depth of $\sim 1\text{--}2$ mm. However, full-range techniques regain their importance in SDM-OCT systems, since it requires a long imaging ranges to separate multi-channel images at different depths. In this paper, we demonstrated a modified SDM-OCT system with full-range imaging capability by simply offsetting the beam at the galvo mirror. Particularly, we systematically characterized phase modulation with respect to various scanning parameters, which is the key to the successful reconstruction of complex interference signals and final full-range images [18–20]. Compared to the standard SDM-OCT, FR-SDM-OCT only utilizes a half sampling rate to cover all path-length-encoded images in the same total imaging range. Thus, the full-range technique can effectively lower the minimum hardware requirements for SDM-OCT technology. Specifically, we can reduce all the following requirements by half: 1) Maximum bandwidth of the dual balanced detector; 2) maximum sampling rate of the digitizer; 3) maximum data transfer rate of the PCI/PCIe bus; 4) data size of the single A-scan; and 5) minimum coherence length of the swept-source laser. All these improvements can yield an increased availability of the hardware to build an SDM-OCT system. From another perspective, the full-range technique can be used to double the image range of SDM-OCT using the same hardware, enabling twice as many parallel imaging channels to be acquired simultaneously at the same data transfer rate.

In our study, complex conjugate rejection ratios (CCRR) were evaluated at different depth ranges for the FR-SDM-OCT system, which was 46.1 dB at ~ 1.4 mm and 30.0 dB at ~ 19.4 mm (see Fig. 4). The measured CCRR values of FR-SDM-OCT were comparable to those CCRR values reported in previous studies using the same galvo-based full-range technique [18,19,21,31], which were between $\sim 30\text{--}40$ dB. We also observed a decreasing trend of CCRR for the FR-SDM-OCT system as the depth range increased, which was consistent with previous studies. Sarunic et al. reported that the CCRR value was 25 dB near zero delay but dropped to 18 dB at ~ 4 mm depth [12]. Wang et al. reported a ~ 40 dB CCRR measured at ~ 100 mm depth and a decreased CCRR value of <20 dB at ~ 700 mm depth [24]. We suspect that the inferior performance of complex conjugate suppression in the FR-SDM-OCT system was due to higher phase instability in the deeper depth ranges. This may be improved by further stabilizing the system with damped vibration. Also, additional software calibration steps can be applied to improve the signals at a deeper depth range [14,24].

The current version of the SDM-OCT has a 6 dB signal loss when the signals are back-propagated through the 1×4 fiber-based SDM component [3–5]. The sensitivity of this 4-beam system, running at 400,000 effective A-scans/s, is still comparable to a single-beam OCT system operating at an A-scan rate of 400,000 A-scans/s and with the same power for each sample beam. The photon loss of the 1×4 splitter was compensated by the 4x increased exposure time at each imaging location enabled by the parallel imaging scheme of SDM-OCT.

In Section 2.3.2, we point out that the SDM-OCT analysis and the galvo-based full-range demodulation analysis can be treated as two independent steps, since the SDM-OCT analysis is performed in k-domain while the full-range analysis is performed in the u-domain. Therefore, employment of the full-range technique does not affect the performance of the SDM-OCT system. In the actual implementation of the full-range technique in our system, given the fixed beam offset and the required scan range, the optimal number of A-scans to achieve best full-range performance may lead to oversampling along fast-axis and longer acquisition time (e.g. $2.2\times$ oversampling for FR-SDM-OCT angiography). This can be improved by choosing a proper beam offset based on Eq. (8) in Section 2.2.

We also demonstrated the feasibility of FR-SDM-OCT angiography (FR-SDM-OCTA) to acquire label-free parallel imaging of the microvascular networks in human fingernails. Prior to our study, angiography has been employed in several multiplexed OCT systems. Two-beam or three-beam Doppler OCT have been established to visualize blood flow at the same spot

from different orientations and reconstruct the directional velocity maps [32,33]. Song et al. reported a Fourier domain multiplexed dual-beam SS-OCTA system [34]. Both SDM-OCTA and dual-beam SS-OCTA utilized the same path-length-encoding technique, which was first introduced by Ifimia et al. in order to reduce the speckles of OCT images [35]. However, SDM-OCTA utilizes only one sample arm to accommodate all channels and performs parallel detection of OCT angiography signals, while the dual-beam SS-OCTA system utilized two sets of sample arms.

The performance of the FR-SDM-OCT system can be further improved by applying the MZI k-clock as the external sampling clock [25,36] to sample the FR-SDM-OCT data, which is widely adopted as a standard technique in SS-OCT systems. Employing this k-clock sampling technique, simultaneous acquisition of MZI signals in the secondary channel of the digitizer is no longer required since obtained SDM-OCT signals are already uniformly sampled in the k-space, which can reduce the signal digitization, processing and storage by half and remove the data resampling post-processing procedure [26,36]. However, the trigger jitter issue still needs to be properly addressed to guarantee the phase stability for the SDM-OCT system.

5. Summary

In summary, we demonstrated a full-range space-division multiplexing optical coherence tomography (FR-SDM-OCT) system. Utilizing a galvanometer-based phase modulation full-range technique, FR-SDM-OCT can be realized to double the depth range of OCT measurements with a complex conjugate rejection ratio of ~ 46.1 dB at ~ 1.4 mm depth and ~ 30.0 dB at ~ 19.4 mm depth, respectively. The feasibility of the FR-SDM-OCT system was demonstrated by imaging Scotch tapes and human fingernails *in vivo*. In addition, FR-SDM-OCT angiography (FR-SDM-OCTA), a functional extension of FR-SDM-OCT, was demonstrated to achieve simultaneous acquisition of human fingernail angiograms from multiple positions. Rich details of microvascular networks in both the proximal nail fold and the nail bed regions were shown in the FR-SDM-OCT angiogram with a field of view of ~ 1.7 mm \times ~ 7.5 mm. Incorporating the full-range technique can effectively alleviate the demanding hardware requirements required by SDM-OCT, which facilitates the adoption of SDM-OCT technology.

Funding

National Science Foundation (DBI-1455613, IIP-1640707); National Institute of Biomedical Imaging and Bioengineering (R01EB025209).

Acknowledgments

We thank Zhao Dong for the helpful discussions of the study.

Disclosures

The authors declare that there are no conflicts of interest related to this article.

References

1. D. Huang, E. A. Swanson, C. P. Lin, J. S. Schuman, W. G. Stinson, W. Chang, M. R. Hee, T. Flotte, K. Gregory, C. A. Puliafito, and J. G. Fujimoto, "Optical coherence tomography," *Science* **254**(5035), 1178–1181 (1991).
2. T. Klein and R. Huber, "High-speed OCT light sources and systems [Invited]," *Biomed. Opt. Express* **8**(2), 828–859 (2017).
3. C. Zhou, A. Alex, J. Rasakanthan, and Y. Ma, "Space-division multiplexing optical coherence tomography," *Opt. Express* **21**(16), 19219–19227 (2013).
4. Y. Huang, M. Badar, A. Nitkowski, A. Weinroth, N. Tansu, and C. Zhou, "Wide-field high-speed space-division multiplexing optical coherence tomography using an integrated photonic device," *Biomed. Opt. Express* **8**(8), 3856–3867 (2017).

5. J. Jerwick, Y. Huang, Z. Dong, A. Slaudades, A. J. Brucker, and C. Zhou, "Wide-field Ophthalmic Space-Division Multiplexing Optical Coherence Tomography," *Photonics Res.* **8**(4), 539–547 (2020).
6. J. F. de Boer, R. Leitgeb, and M. Wojtkowski, "Twenty-five years of optical coherence tomography: the paradigm shift in sensitivity and speed provided by Fourier domain OCT [Invited]," *Biomed. Opt. Express* **8**(7), 3248–3280 (2017).
7. M. Wojtkowski, A. Kowalczyk, R. Leitgeb, and A. F. Fercher, "Full range complex spectral optical coherence tomography technique in eye imaging," *Opt. Lett.* **27**(16), 1415–1417 (2002).
8. Y. Yasuno, S. Makita, T. Endo, G. Aoki, H. Sumimura, M. Itoh, and T. Yatagai, "One-shot-phase-shifting Fourier domain optical coherence tomography by reference wavefront tilting," *Opt. Express* **12**(25), 6184–6191 (2004).
9. S. H. Yun, G. J. Tearney, J. F. de Boer, and B. E. Bouma, "Removing the depth-degeneracy in optical frequency domain imaging with frequency shifting," *Opt. Express* **12**(20), 4822–4828 (2004).
10. J. G. Zhang, J. S. Nelson, and Z. Chen, "Removal of a mirror image and enhancement of the signal-to-noise ratio in Fourier-domain optical coherence tomography using an electro-optic phase modulator," *Opt. Lett.* **30**(2), 147–149 (2005).
11. Z. Wang, H.-C. Lee, D. Vermeulen, L. Chen, T. Nielsen, S. Y. Park, A. Ghaemi, E. Swanson, C. Doerr, and J. Fujimoto, "Silicon photonic integrated circuit swept-source optical coherence tomography receiver with dual polarization, dual balanced, in-phase and quadrature detection," *Biomed. Opt. Express* **6**(7), 2562–2574 (2015).
12. M. V. Sarunic, M. A. Choma, C. Yang, and J. A. Izatt, "Instantaneous complex conjugate resolved spectral domain and swept-source OCT using 3×3 fiber couplers," *Opt. Express* **13**(3), 957–967 (2005).
13. B. J. Vakoc, S. H. Yun, G. J. Tearney, and B. E. Bouma, "Elimination of depth degeneracy in optical frequency-domain imaging through polarization-based optical demodulation," *Opt. Lett.* **31**(3), 362–364 (2006).
14. M. Siddiqui, S. Tozburun, E. Z. Zhang, and B. J. Vakoc, "Compensation of spectral and RF errors in swept-source OCT for high extinction complex demodulation," *Opt. Express* **23**(5), 5508–5520 (2015).
15. Y. Yasuno, S. Makita, T. Endo, G. Aoki, M. Itoh, and T. Yatagai, "Simultaneous B-M-mode scanning method for real-time full-range Fourier domain optical coherence tomography," *Appl. Opt.* **45**(8), 1861–1865 (2006).
16. S. Makita, T. Fabritius, and Y. Yasuno, "Full-range, high-speed, high-resolution 1- μ m spectral-domain optical coherence tomography using BM-scan for volumetric imaging of the human posterior eye," *Opt. Express* **16**(12), 8406–8420 (2008).
17. M. Yamanari, S. Makita, Y. Lim, and Y. Yasuno, "Full-range polarization-sensitive swept-source optical coherence tomography by simultaneous transversal and spectral modulation," *Opt. Express* **18**(13), 13964–13980 (2010).
18. B. Baumann, M. Pircher, E. Götzinger, and C. K. Hitzenberger, "Full range complex spectral domain optical coherence tomography without additional phase shifters," *Opt. Express* **15**(20), 13375–13387 (2007).
19. R. A. Leitgeb, R. Michaely, T. Lasser, and S. C. Sekhar, "Complex ambiguity-free Fourier domain optical coherence tomography through transverse scanning," *Opt. Lett.* **32**(23), 3453–3455 (2007).
20. L. An and R. K. Wang, "Use of a scanner to modulate spatial interferograms for in vivo full-range Fourier-domain optical coherence tomography," *Opt. Lett.* **32**(23), 3423–3425 (2007).
21. H. Kawagoe, M. Yamanaka, S. Makita, Y. Yasuno, and N. Nishizawa, "Full-range ultrahigh-resolution spectral-domain optical coherence tomography in 1.7 μ m wavelength region for deep-penetration and high-resolution imaging of turbid tissues," *Appl. Phys. Express* **9**(12), 127002 (2016).
22. R. Motaghiannezam and S. Fraser, "Logarithmic intensity and speckle-based motion contrast methods for human retinal vasculature visualization using swept source optical coherence tomography," *Biomed. Opt. Express* **3**(3), 503–521 (2012).
23. M. Guizar-Sicairos, S. T. Thurman, and J. R. Fienup, "Efficient subpixel image registration algorithms," *Opt. Lett.* **33**(2), 156–158 (2008).
24. Z. Wang, B. Potsaid, L. Chen, C. Doerr, H.-C. Lee, T. Nielsen, V. Jayaraman, A. E. Cable, E. Swanson, and J. G. Fujimoto, "Cubic meter volume optical coherence tomography," *Optica* **3**(12), 1496–1503 (2016).
25. W. Choi, B. Potsaid, V. Jayaraman, B. Baumann, I. Grulkowski, J. J. Liu, C. D. Lu, A. E. Cable, D. Huang, J. S. Duker, and J. G. Fujimoto, "Phase-sensitive swept-source optical coherence tomography imaging of the human retina with a vertical cavity surface-emitting laser light source," *Opt. Lett.* **38**(3), 338–340 (2013).
26. S. Moon and Z. Chen, "Phase-stability optimization of swept-source optical coherence tomography," *Biomed. Opt. Express* **9**(11), 5280–5295 (2018).
27. H. C. Hendargo, R. P. McNabb, A.-H. Dhalla, N. Shepherd, and J. A. Izatt, "Doppler velocity detection limitations in spectrometer-based versus swept-source optical coherence tomography," *Biomed. Opt. Express* **2**(8), 2175–2188 (2011).
28. B. Hofer, B. Považay, B. Hermann, A. Unterhuber, G. Matz, and W. Drexler, "Dispersion encoded full range frequency domain optical coherence tomography," *Opt. Express* **17**(1), 7–24 (2009).
29. S. Sangiorgi, A. Manelli, T. Congiu, A. Bini, G. Pilato, M. Reguzzoni, and M. Raspanti, "Microvascularization of the human digit as studied by corrosion casting," *J. Anat.* **204**(2), 123–131 (2004).
30. U. Baran, L. Shi, and R. K. Wang, "Capillary blood flow imaging within human finger cuticle using optical microangiography," *J. Biophotonics* **8**(1-2), 46–51 (2015).
31. Q. Li, K. Karnowski, M. Villiger, and D. D. Sampson, *Local birefringence of the anterior segment of the human eye in a single capture with a full range polarisation-sensitive optical coherence tomography*, International Conference on Biophotonics V (SPIE, 2017), Vol. 10340, p. 1.

32. S. Zotter, M. Pircher, T. Torzicky, M. Bonesi, E. Goetzinger, R. A. Leitgeb, and C. K. Hitzenberger, "Visualization of microvasculature by dual-beam phase-resolved Doppler optical coherence tomography," *Opt. Express* **19**(2), 1217–1227 (2011).
33. W. Träsichker, R. M. Werkmeister, S. Zotter, B. Baumann, T. Torzicky, M. Pircher, and C. K. Hitzenberger, "In vitro and in vivo three-dimensional velocity vector measurement by three-beam spectral-domain Doppler optical coherence tomography," *J. Biomed. Opt.* **18**(11), 116010 (2013).
34. S. Song, J. Xu, and R. K. Wang, "Flexible wide-field optical micro-angiography based on Fourier-domain multiplexed dual-beam swept source optical coherence tomography," *J. Biophotonics* **11**(3), e201700203 (2018).
35. N. Iftimia, B. E. Bouma, and G. J. Tearney, *Speckle reduction in optical coherence tomography by "path length encoded" angular compounding* (SPIE, 2003), Vol. 8, pp. 260–263, 264.
36. J. Xi, L. Huo, J. Li, and X. D. Li, "Generic real-time uniform K-space sampling method for high-speed swept-Source optical coherence tomography," *Opt. Express* **18**(9), 9511–9517 (2010).